Photoluminescence Quenching in WSe_2 via p-Doping Induced by Functionalized Rylene Dyes

Ana M. Valencia,[a] Theresa Kuechle,[b] Maximiliam Tomoscheit,[b] Sarah Jasmin Finkelmeyer,[c] Olga Utismenko,[d], Kalina Peneva,[d,e] Martin Presselt,[c,e,f] Giancarlo Soavi,[b,g] and Caterina Cocchi,[a,h]

Hybrid heterostructures combining transition metal dichalcogenides (TMDs) with light-harvesting dyes are promising materials for next-generation optoelectronics. Yet, controlling and understanding interfacial charge transfer mechanisms in these complex systems remains a major challenge. Here, we investigate the microscopic origin of photoluminescence (PL) quenching in WSe_2 functionalized with a novel, strongly electron-deficient perylene monoimide dye, CN_4PMI. Experimentally, the hybridization induces a $\sim$97% PL quenching in WSe_2, confirming substantial static charge transfer and increased p-doping from the dye. To isolate the dominant electronic mechanism, we investigate from first principles various interface morphologies, including differing molecular orientations and layer thicknesses. Our density-functional theory results confirm that CN_4PMI acts as a strong electron acceptor, inducing p-doping and forming a type-II level alignment with all considered configurations, giving rise to a small or vanishing band gap. Based on these findings, we attribute the observed PL suppression in WSe_2 to these strong electronic interactions with the dye. Our study provides a clear and validated strategy for tailoring the electronic structure of TMDs through targeted, electron-deficient organic functionalization.

1 Introduction

The combination of light-harvesting dyes and transition metal dichalcogenide (TMD) monolayers, an established family of low-dimensional semiconductors exhibiting excellent transport properties,[1–3] a rich exciton physics,[4,5] and efficient photoluminescence (PL),[6–10] is expected to unite the best of two worlds.[11,12] These hybrid heterostructures promise a new class of materials for next-generation optoelectronic[13,14] and photonic[15] applications. To achieve this ambitious goal, a deep understanding of the fundamental processes that govern the interaction between dyes and TMDs is mandatory.

Molecular adsorption is a viable tool to tune the optical properties of TMDs,[16–18] leading to both PL enhancement or suppression depending on the specific characteristics of the heterostructure.[19–21] On one hand, PL can be enhanced when molecular adsorbates[22–24] or solvent molecules[25] heal detrimental defects[26] within the TMD lattice. On the other hand, PL is typically suppressed, primarily due to two concurrent effects related to charge transfer: spatial separation of photoinduced charge carriers,[27] and doping, either from a substrate[24,28] or within a heterointerface,[29,30] both decreasing the probability of radiative recombination.[31,32] Effective charge transfer, associated with a type-II level alignment, is known to reduce the inherent TMD PL.[33,34] Given the complexity of these competing mechanisms and the large variety of parameters that can influence the optical properties, a systematic, targeted analysis is urgently needed to isolate and understand the dominant effect.

To better understand the PL suppression scenario and investigate charge transfer mechanisms at organic-inorganic interfaces, we specifically designed a novel perylene monoimide dye functionalized with four cyano groups (CN_4PMI) at the bay positions. Cyano groups are well-known for their strong electron-withdrawing character,[35] which significantly lowers the LUMO energy level of the molecule, thus enhancing its electron affinity.[36] This molecular design, which builds upon strategies commonly used in organic photovoltaics to tailor energy levels and enable type-II band alignment,[37–39] enables CN_4PMI to efficiently accept electrons from WSe_2 and promote p-type doping in the TMD. Furthermore, the compact and planar nature of the cyano substituents preserves the molecular π-system, supporting strong $\pi-\pi$ interactions and a flat-lying adsorption geometry, both of which favor charge transfer at the interface.[40,41]

Acknowledging the inherent experimental difficulties in synthesizing well-ordered samples and obtaining precise information about their morphology and composition, we use density-functional theory (DFT) as an ideal guide to rationalize PL quenching mechanisms measured in a hybrid heterostructure formed by WSe_2 decorated by CN_4PMI molecules. We explore different configurations with varying substrate, molecular film thickness, and organic layer orientations. Molecular adsorption is stable in all considered conditions, but it is particularly favored when the dyes lie flat on the substrate. Due to its electron-acceptor nature, CN_4PMI induces strong p-doping on WSe_2, leading to a type-II level alignment and a narrow (< 500meV) or vanishing band gap. The strong electronic interactions between adsorbate and substrate, regardless of the specific characteristics of the hybrid interface, strongly point to their role as the driving mechanism for the observed PL quenching in WSe_2.

[a] *Institute of Physics, Carl-von-Ossietzky Universität Oldenburg, 26129 Oldenburg, Germany; E-mail: ana.valencia@uni-oldenburg.de*

[b] *Institute of Solid State Physics, Friedrich-Schiller-Universität Jena, 07743 Jena, Germany.*

[c] *Leibniz Institute of Photonic Technology, 07745 Jena, Germany.*

[d] *Institute of Organic Chemistry and Macromolecular Chemistry, Friedrich-Schiller-Universität Jena, 07743 Jena, Germany.*

[e] *Center for Energy and Environmental Chemistry Jena (CEEC Jena), Friedrich Schiller Universität Jena, 07743 Jena, Germany.*

[f] *sciclus GmbH & Co. KG, 07745 Jena, Germany.*

[g] *Abbe Center of Photonics, Friedrich-Schiller-Universität Jena, 07743 Jena, Germany.*

[h] *Institute of Condensed Matter Theory and Optics, Friedrich-Schiller-Universität Jena, 07743 Jena, Germany ; E-mail:caterina.cocchi@uni-jena.de.*

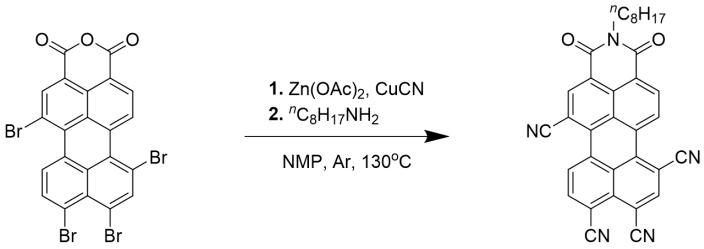

Fig. 1 Synthesis of CN_4PMI.

2 Materials and Methods

2.1 Synthesis

The CN_4PMI dye was synthesized via a one-pot two-step procedure starting from tetrabromo-perylene-3,4:9,10-tetracarboxylic monoanhydride (PMA-4Br). First, the precursor was subjected to nucleophilic aromatic substitution with copper(I) cyanide (CuCN) in the presence of zinc acetate in dry N-methyl-2-pyrrolidone (NMP) at 130°C under an inert atmosphere. This reaction substituted the four bromine atoms at the bay positions with cyano groups, yielding a tetra-cyano-substituted perylene monoanhydride intermediate. N-octylamine was then added directly, promoting imidization under the same conditions and forming the monoimide product in situ. The crude product was isolated by precipitation, followed by purification via silica gel column chromatography. The structure of CN_4PMI was confirmed by NMR spectroscopy and high-resolution mass spectrometry, consistent with complete substitution at the bay positions and successful monoimide formation. The resulting molecule is highly planar, displays strong absorption in the visible range, and retains luminescent properties in dilute solution. Further details are provided in the Electronic Supplementary Information (ESI).

2.2 Experimental Methods

2.2.1 Mechanical exfoliation of WSe_2 monolayer

The WSe_2 flakes were fabricated by mechanical exfoliation. As a first step, bulk material was thinned down before being exfoliated one more time onto a PDMS film. Through optical microscopy contrast, areas of a single layer were identified and subsequently positioned over a Si/SiO_2 substrate using a mechanical xyz stage. The viscoelastic properties of the PDMS allow for a careful separation from the monolayer, while keeping it intact. To increase the likelihood of a successful transfer, the system was slowly heated to 60 °C.

2.2.2 Langmuir-Blodgett method

A UV-Vis absorption and emission spectrum of a CN_4PMI chloroform solution can be found in Fig. 2a. The surface pressure (mean molecular area) (II(mma)) isotherm of CN_4PMI was recorded after spreading 1500 μL of 0.1 μmol/mL chloroform solution there of (kept at room temperature, RT) onto a 25°C tempered-controlled pure water (0.16 to 0.25 μS/cm) subphase in an LB trough (KSV 5000, length = 520 mm, compression length=475.2 mm, width=150 mm).To allow complete solvent evaporation, 20 minutes are granted before starting barrier movement. The barriers were moved at a maximum rate of 10 mm/min, with an additional rate limitation of 5 mN/m/min. The higher rate was applied while the surface pressure remained constant; when the surface pressure began to rise, the rate limitation was enforced.

For the Langmuir monolayer deposition of CN4PMI, the same conditions as for recording the isotherm were applied. The Langmuir layers were deposited via the LB technique at a surface pressure of 30 mN/m, which corresponds to a dense packing of perylenes.[42]

2.2.3 Brewster angle microscopy (BAM)

Brewster angle microscopy (BAM) images were recorded using a KSV NIMA MicroBAM (Biolin Scientific) before spreading (pure water subphase), after spreading, during the solvent evaporation period, and periodically throughout all stages of the II(mma) isotherm measurement.[43]

2.2.4 PL setup

For the excitation of the samples, we used a continuous wave (CW) laser system (MixTrain from Spectra-Physics) with tunable output in the wavelength range from 515 to 670 nm. The excitation beam is then coupled to a custom-built microscope via a 90:10 beam splitter, and subsequently it is focused on the sample using an objective (Mitutoyo M Plan Apo HL, 50x) which allows for obtaining a $1/e^2$ spot size at the sample position of approximately 1.59 μm at 633 nm. The back-scattered PL signal is passed through the same objective and, after filtering using notch filters to remove the excitation beam, it is directed to a monochromator (Horiba iHR550) equipped with an electrically cooled CCD camera (SynapsePlus detector) for low-noise detection.

2.3 Computational Details

All calculations presented in this work are carried out in the framework of DFT, using the all-electron code FHI-aims[44] in the scalar relativistic approximation. The heterostructures are relaxed using the Perdew-Burke-Ernzerhof (PBE) exchange-correlation functional[45] supplemented by the pairwise Tkatchenko-Scheffler scheme[46] for dispersion corrections. A dipole correction is included to prevent spurious electrostatic interactions between the periodic replicas of the simulation cells, including a 60 Å thick vacuum layer. The electronic properties are subsequently computed with the range-separated hybrid functional HSE06[47] including spin-orbit coupling. "Tight" numerical settings are used for the PBE calculations, while the "LVL-intermediate" settings are employed with HSE06. Brillouin zone integrations are performed using a Monkhorst-Pack **k**-mesh with $12\times12\times1$ points for the primitive cell of WSe_2 and $6\times3\times1$ for the hybrid interfaces simulated in supercells. Convergence criteria are set to 10^{-6} eV for the total energy and 10^{-5} for changes in the density matrix. Structural relaxations are carried out until the forces on all atoms are below 0.001 eV/Å.

3 Results

3.1 PL spectroscopy

We start our analysis by comparing the PL spectra of the hybrid CN_4PMI-WSe_2 interfaces with those of pristine WSe_2 taken on the

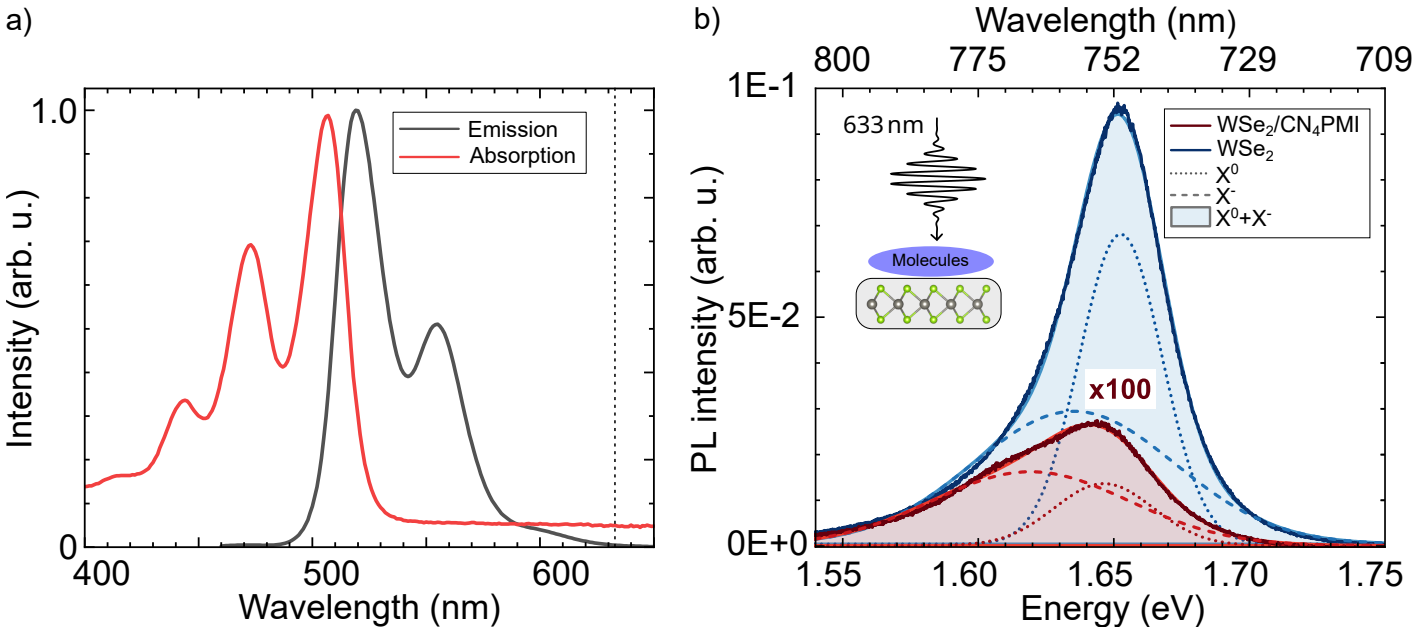

Fig. 2 a) UV-Vis absorption (red curve) and emission (black curve) spectrum of the CN_4PMI molecule b) PL spectra of a pristine WSe_2 monolayer (blue curve) and the same sample after hybridization with CN_4PMI (red curve), both exited with the same laser power density of 5000 W/cm^2 and wavelength of 633 nm.

same sample before and after CN_4PMI deposition (Fig. 2b). For these measurements, we used an excitation wavelength of 633 nm at an average power density of 5000 W/cm^2. The hybridization process in the heterostructure results in two main spectral changes in WSe_2. First, we observe a strong reduction of the PL intensity by $\sim 97\%$, which can have both a static or dynamic origin, similar to previous findings for TMD-graphene heterostructures.[48] Static charge transfer due to hybridization leads to doping in the TMD, and thus to a higher trion density, which typically displays very low PL yield due to ultrafast non-radiative recombination pathways.[49,50] On the other hand, ultrafast charge transfer following photoexcitation can reduce the number of available electron-hole pairs, which are necessary for radiative recombination.

Another drastic difference in the PL spectra linked to the previous discussion is the change in the trion density. To estimate the exciton/trion ratio, we applied a cumulative Gaussian fit for the neutral A exciton peak at higher (1.665 eV for the pristine sample and 1.650 eV for the hybridized sample) and the trion peak at lower (1.647 eV for the pristine and 1.640 eV for the hybridized sample) energies.[51] The exciton/trion ratio changes from 0.88 for the pristine WSe_2 to 0.28 for the hybrid CN_4PMI-WSe_2 sample. This increase in the trion density suggests the presence of a strong static charge transfer from the CN_4PMI molecule to the monolayer WSe_2[52] immediately after adsorption, in agreement with previous reports on WSe_2-perylene hybrids.[53] Furthermore, we observe a redshift by approximately 6-9 meV of the PL peaks from pristine to hybrid samples for the neutral exciton and trion, respectively, possibly indicating the concomitant effect of charge transfer and dielectric screening.

Overall, our experimental comparison of the PL spectra in pristine WSe_2 and hybrid CN_4PMI-WSe_2 samples delivers two main findings: a reduction of the exciton/trion ratio and a concomitant overall quenching of the PL intensity. Both observations can be rationalized in the context of a type-II band alignment, which could be responsible for both a static charge transfer immediately after hybridization and a dynamical photo-induced doping, leading to an overall reduction of the PL intensity due to the presence of additional non-radiative recombination channels. To confirm this hypothesis, we investigate in detail the band alignment of the CN_4PMI-WSe_2 hybrid interfaces from DFT.

Table 1 Adsorption energy, minimal distance (d) between adsorbed molecule and substrate, charge transfer (CT) from WSe_2 to the organic layer, and energy gap of the hybrid interfaces modeled in this work

System	E_{ads} [eV]	d [Å]	CT [e]	E_{gap} [eV]
CN_4PMI@1L	-2.42	3.52	0.23	0.50
CN_4PMI@2L	-2.46	3.59	0.22	0.47
CN_4PMI@3L	-2.47	3.48	0.22	0.41
2(CN_4PMI)@1L	-2.60	3.65	0.31	0.00
CN_4PMI(22°)@1L	-1.15	3.16	0.07	0.19
CN_4PMI(43°)@1L	-0.58	2.70	0.07	0.00

3.2 Computational Analysis

We model the CN_4PMI-WSe_2 heterostructure assuming six different setups with varying numbers of layers and molecular orientations. We consider three configurations with CN_4PMI adsorbed flat on a WSe_2 monolayer (Fig. 3a) or with an angle of 22° and 43° (Fig. 3b and Fig. 3c, respectively). To address the influence of organic film thickness, we additionally simulate two CN_4PMI lying flat on monolayer WSe_2 (Fig. 3d), while to assess the impact of the number of TMD layers, we investigate CN_4PMI adsorbed flat on bilayer and trilayer WSe_2, see Fig. 3e and f, respectively.

To evaluate the interactions between adsorbed molecules and

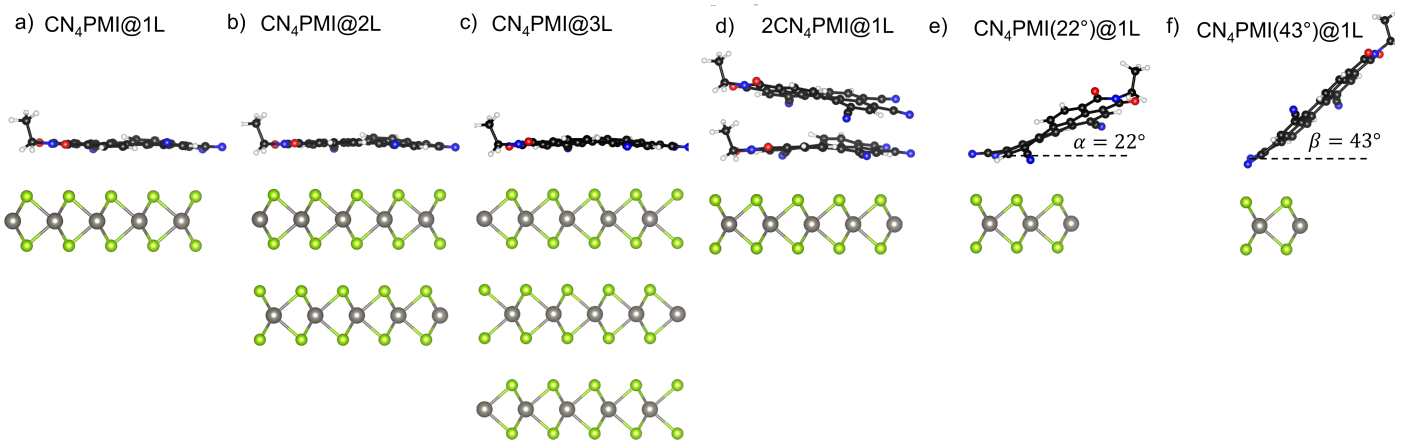

Fig. 3 Ball-and-stick representations, created with the visualization software VESTA,[54] of the unit cells of the investigated hybrid interfaces, including a single CN_4PMI adsorbed flat on a) monolayer, b) bilayer, and c) trilayer WSe_2, d) CN_4PMI molecules adsorbed on WSe_2 monolayer and a single CN_4PMI molecule adsorbed on monolayer WSe_2 with an angle e) $\alpha = 22°$ and f) $\beta = 43°$. C, N, O, H, W, and Se atoms are depicted in black, blue, red, white, gray, and green, respectively.

the underlying WSe_2 substrate, we calculate from DFT the adsorption energy as the difference between the total energy of the hybrid interface and the total energies of its separate constituents in their optimized geometries:

$$E_{\text{ads}} = E_{\text{hybrid}} - nE_{WSe_2} - mE_{\text{dye}}. \quad (1)$$

In Eq. (1), n and m indicate the number of TMD and organic layers, respectively, that are present in each considered heterostructure. As summarized in Table 1, all computed adsorption energies are negative and have a magnitude larger than 0.5 eV, suggesting favorable adsorption in all configurations. However, a more careful inspection reveals important differences according to the interface morphology. When the molecules lie flat on WSe_2, the adsorption energies assume the largest values, of the order of -2.50 eV. This is due to the strong interactions between the extended carbon-conjugated network of CN_4PMI and the TMD surface, as further testified by the interfacial distance d of about 3.5 Å, which is almost independent of the number of TMD layers (Table 1).

The adsorption of two molecules on a WSe_2 monolayer is more favorable by about 100 meV than single-molecule adsorption, despite the strong intermolecular couplings incrementing the distance between molecule and substrate to 3.65 Å. Non-recumbent molecules adsorb less favorably on WSe_2 (Table 1), due to the substantial reduction of π-π interactions between adsorbate and substrate. In these configurations, where the CN_4PMI forms an angle of 22° and 43° with WSe_2, the interaction with the TMD occurs via the N atom at the edge, leading to a reduced separation as the angle increases. The adsorption energy decreases accordingly, down to -1.15 eV and -0.58 eV upon 22° and 43° angles, respectively (Table 1).

Additional information about substrate-molecule interactions in these heterostructures can be gained by evaluating the degree of interfacial charge transfer (CT) from partial charge analysis, performed here adopting the Hirshfeld scheme.[55] As summarized in Table 1, the CT trends follow those of the adsorption energies and minimal distances. When the dyes are adsorbed flat on WSe_2, they withdraw 0.22 e, regardless of the number of underlying TMD layers. Two molecules adsorbed on WSe_2 monolayer attract more than 0.3 e, confirming the strongest interaction obtained in this setting. Intermolecular CT in this heterostructure amounts to 0.05 e, which, interestingly, almost entirely compensates the difference with the CT induced by a single adsorbed dye. This result suggests that intermolecular interactions enhance interfacial couplings. Conversely, non-recumbent molecular adsorption leads to an electron transfer of only 0.07 e, reiterating the key role of π-interactions, which are minimized there.

The non-negligible CT between CN_4PMI and WSe_2, which becomes larger with increasing interfacial interactions between the building blocks, is further confirmed by the analysis of the PDOS (Fig. 4). The lowest unoccupied molecular orbital (LUMO) of the molecule is found within the WSe_2 gap in all considered configurations, which is a clear signature of electron doping induced by the molecule. All heterostructures are thus characterized by a type-II level alignment, with the highest occupied level corresponding to the valence-band maximum (VBM) of WSe_2 and the lowest unoccupied state by the LUMO of CN_4PMI. The size of the fundamental gap varies with the interface morphology. As reported in Table 1, a single dye adsorbed flat on monolayer WSe_2 is characterized by the largest gap of 0.5 eV. This magnitude decreases with the number of underlying TMD layers, leading to 0.47 eV (0.41 eV) for the bilayer (trilayer) substrate. Detailed inspection of the PDOS reveals that the largest band gap in the CN_4PMI@1L heterostructure is due to the maximized upshift of the LUMO energy compared to its value in the isolated molecule (Fig. 4a). The magnitude of this shift decreases with the number of underlying WSe_2 layers (Fig. 4b,c) as a result of reduced polarization induced by the substrate. It is worth noting that the band edges of WSe_2 monolayer undergo almost no shift in the presence of a single adsorbate (Fig. 4a).

In the hybrid interfaces with bilayer and trilayer substrates, both the VBM and the conduction band minimum (CBm) of WSe_2 upshift by $\sim$100 meV upon CN_4PMI adsorption. The highest-occupied molecular orbital (HOMO) of the dye appears around

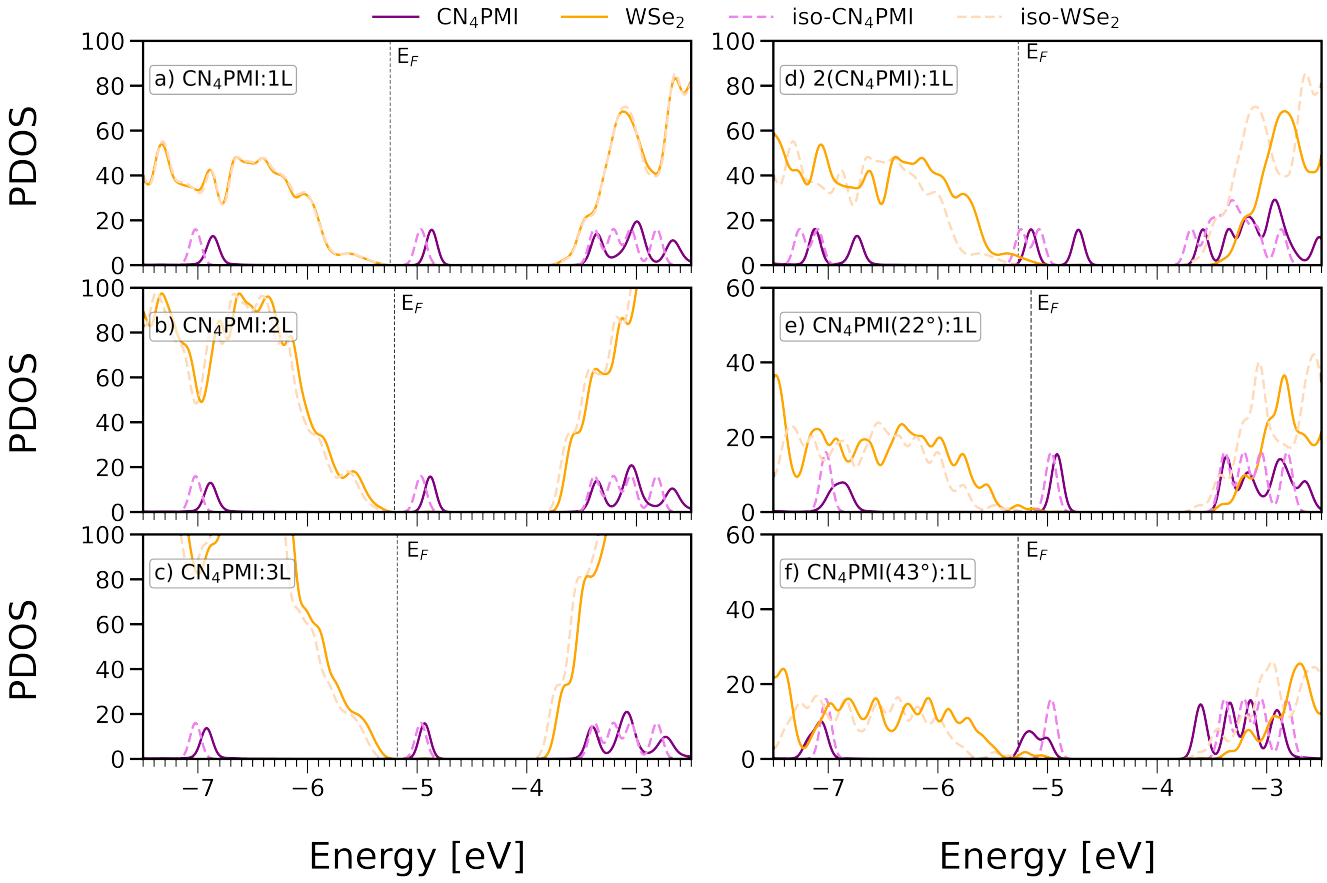

Fig. 4 Projected densities of state (PDOS) of CN_4PMI adsorbed on WSe_2 in all considered configurations: a) CN_4PMI:1L, b) CN_4PMI:2L, c) CN_4PMI:3L, d) 2(CN_4PMI):1L, e) CN_4PMI(22°):1L, and f) CN_4PMI(43°):1L. The contributions from molecule (purple) and WSe_2 (orange) in the heterostructure are indicated by solid curves, while the results obtained for the isolated constituents are plotted by dashed curves (CN_4PMI in magenta and WSe_2 in light orange). A 50 meV Lorentzian broadening is applied to all curves for visualization. The energy scale is referenced to the vacuum level, and the Fermi energy (E_F) is marked by a dotted bar.

-7 eV in the PDOS reported in Fig. 4a-c. Similar to the LUMO, its energy undergoes an increasing upshift with decreasing number of WSe_2 substrate layers. However, neither the HOMO nor the LUMO of CN_4PMI carry signatures of hybridization, in line with the rationale elaborated for non-functionalized rylene dyes on TMDs[56]. On the other hand, as expected[56], the higher unoccupied molecular orbitals appear hybridized with the substrate, as indicated by the modified shape of the corresponding band appearing between -3.5 eV and -2.5 eV in the isolated and adsobrd dye (Fig. 4a-c, dashed magenta *vs.* solid purple curves).

The stronger interactions induced by two π-stacked dyes[57] on top of monolayer WSe_2 are also reflected in the electronic structure of the corresponding interface (Fig. 4d). As a result of strong doping, which sizeably upshifts the VBM of WSe_2 by about 300 meV, this system is metallic (Table 1). The strong interfacial interactions also lead to a splitting of both the HOMO and LUMO of the dyes, which become energetically close to those in the isolated dimer (Fig. S4). Hybridization and polarization effects are quite pronounced in the unoccupied region of both constituents. Similar to the valence band, the conduction band of the TMD is also upshifted by more than 300 meV, while the unoccupied molecular orbitals are substantially reorganized upon adsorption (Fig. 4d).

Non-recumbent adsorption, while being energetically less favorable and leading to reduced CT than the flat configurations, induces non-negligible modifications in the electronic structure of both constituents (Fig. 4e,f). Molecular adsorption with a 22° angle leads to a semiconducting heterostructure with a fundamental gap of 0.19 eV (Table 1). While the LUMO of CN_4PMI is almost unaffected by the presence of the substrate, undergoing a rigid upshift of a few tens of meV, the HOMO strongly hybridizes with the valence bands of WSe_2 (Fig. 4e). The PDOS of the TMD is subject to an upshift of $\sim$250 meV, leading to the sizeable reduction of the band gap compared to the configurations with flat molecules. When the angle between CN_4PMI and WSe_2 increases to 43°, the changes in the electronic structure of the constituents become even larger (Fig. 4f). The LUMO of the molecule is smeared and energetically downshifted, overlapping with the upshifted VBM of WSe_2. These concurrent effects give rise to a metallic heterostructure (Table 1). The HOMO of CN_4PMI is also smeared upon adsorption, while the higher unoccupied levels are decreased in energy by $\sim$250 meV. A similar shift but toward higher energies is present in both the valence and conduction band of WSe_2 (Fig. 4f). Since the CT in the non-recumbent configurations is considerably smaller than upon flat molecular adsorption (Table 1), we conclude that these strong electronic modifications at the interface are due to polarization and local interactions with the N atom at the edge of CN_4PMI, mostly interacting with the upper Se atomic layer in the TMD.

4 Discussion and Conclusions

Quenched PL observed in our experiments is directly related to the strong electronic interactions between CN_4PMI dyes and monolayer/multilayer WSe_2, as revealed by DFT calculations. As extensively discussed in the literature on a variety of interfaces with organic molecules[33,58,59] and inorganic substrates,[24,28] CT and doping are considered detrimental to the intrinsic optical activity of TMDs. Both effects manifest themselves particularly in the presence of a type-II level alignment, leading to a small band gap. Our comprehensive first-principles analysis confirms this hypothesis across various interfacial morphologies. Although flat molecular adsorption is energetically and electronically superior, even non-recumbent orientations induce modifications leading to sizable PL quenching. These results underscore the role of molecular design in modulating the interfacial electronic landscape.[60] In particular, the use of electron-deficient CN_4PMI, featuring multiple cyano substituents, enables efficient charge transfer and energetic alignment with WSe_2. The planarity and high electron affinity of the dye are key features that enable efficient charge transfer and fine-tuning of the TMD band structure via non-covalent interactions.

In conclusion, we attribute the observed PL quenching in WSe_2 decorated by functionalized rylene dyes to p-doping induced by the latter. *Ab initio* calculations, performed for varying molecular coverage and orientation, confirm the robustness of this predicted mechanism. The adsorbed dyes consistently accept electrons from WSe_2, suggesting that in real samples, the available charge fills Se vacancy states, thereby suppressing PL. Beyond explaining this quenching within the broader context of TMD heterostructures, our findings demonstrate a clear pathway for tailoring the electronic structure of these low-dimensional semiconductors via controlled organic functionalization, opening avenues for advanced optoelectronics, nonlinear optics, and quantum technologies.

Conflicts of interest

The authors declare no competing financial or personal conflict of interest regarding this work, except that the company SciClus GmbH & Co. KG (founded by author MP) provided IT infrastructure free of charge for the research. However, this company derived no financial or non-financial benefit from the research and was not involved in the study's design, data collection, analysis, or interpretation, or in the writing of the manuscript.

Data availability

All data produced in this work are available free of charge at `https://doi.org/10.5281/zenodo.17294219`.

Acknowledgements

The authors thank Benedikt Callies for support with the cyclic voltammetry measurements. This work was funded by the German Federal Ministry of Education and Research (Professorinnenprogramm III), the State of Lower Saxony (Professorinnen für Niedersachsen), and the German Research Foundation via the CRC 1375 NOA (project number 398816777, subprojects A8 and B5). Computational resources were provided by the North-German Supercomputing Alliance (HLRN), project bep00132, and by the high-performance computing cluster CARL at the University of Oldenburg, funded by the German Research Foundation (Project No. INST 184/157-1 FUGG) and by the Ministry of Science and Culture of Lower Saxony. KP acknowledges the German Research Foundation for funding in the framework of FOR5301 "FuncHeal" (project number 455748945, project P3).

Notes and references

1 S. M. Eichfeld, L. Hossain, Y.-C. Lin, A. F. Piasecki, B. Kupp, A. G. Birdwell, R. A. Burke, N. Lu, X. Peng, J. Li *et al.*, *ACS Nano*, 2015, **9**, 2080–2087.

2 E. Ponomarev, A. Pasztor, A. Waelchli, A. Scarfato, N. Ubrig, C. Renner and A. F. Morpurgo, *ACS Nano*, 2018, **12**, 2669–2676.

3 N. D. Hien, C. V. Nguyen, N. N. Hieu, S. Kubakaddi, C. Duque, M. Mora-Ramos, L. Dinh, T. N. Bich and H. V. Phuc, *Phys. Rev. B*, 2020, **101**, 045424.

4 G. Wang, A. Chernikov, M. M. Glazov, T. F. Heinz, X. Marie, T. Amand and B. Urbaszek, *Rev. Mod. Phys.*, 2018, **90**, 021001.

5 E. C. Regan, D. Wang, E. Y. Paik, Y. Zeng, L. Zhang, J. Zhu, A. H. MacDonald, H. Deng and F. Wang, *Nat. Rev. Mater.*, 2022, **7**, 778–795.

6 A. Splendiani, L. Sun, Y. Zhang, T. Li, J. Kim, C.-Y. Chim, G. Galli and F. Wang, *Nano Lett.*, 2010, **10**, 1271–1275.

7 G. Eda, H. Yamaguchi, D. Voiry, T. Fujita, M. Chen and M. Chhowalla, *Nano Lett.*, 2011, **11**, 5111–5116.

8 P. Tonndorf, R. Schmidt, P. Böttger, X. Zhang, J. Börner, A. Liebig, M. Albrecht, C. Kloc, O. Gordan, D. R. Zahn *et al.*, *Org. Electron.*, 2013, **21**, 4908–4916.

9 M. Amani, D.-H. Lien, D. Kiriya, J. Xiao, A. Azcatl, J. Noh, S. R. Madhvapathy, R. Addou, S. Kc, M. Dubey *et al.*, *Science*, 2015, **350**, 1065–1068.

10 W. Shi, M.-L. Lin, Q.-H. Tan, X.-F. Qiao, J. Zhang and P.-H. Tan, *2D Mater.*, 2016, **3**, 025016.

11 N. Koch, *Appl. Phys. Lett.*, 2021, **119**, 260501.

12 F. Cui, V. Garcia-Lopez, Z. Wang, Z. Luo, D. He, X. Feng, R. Dong and X. Wang, *Chem. Rev.*, 2024, **125**, 445–520.

13 M. Gobbi, E. Orgiu and P. Samorì, *Adv. Mater.*, 2018, **30**, 1706103.

14 J. Ji and J. H. Choi, *Nanoscale*, 2022, **14**, 10648–10689.

15 F. J. Garcia-de Abajo, D. N. Basov, F. H. L. Koppens, L. Orsini, M. Ceccanti, S. Castilla, L. Cavicchi, M. Polini, P. A. D. Goncalves, A. T. Costa, N. M. R. Peres, N. A. Mortensen, S. Bharadwaj, Z. Jacob, P. J. Schuck, A. N. Pasupathy, M. Delor, M. K. Liu, A. Mugarza, P. Merino, M. G. Cuxart, E. Chavez-Angel, M. Svec, L. H. G. Tizei, F. Dirnberger, H. Deng, C. Schneider, V. Menon, T. Deilmann, A. Chernikov, K. S. Thygesen, Y. Abate, M. Terrones, V. K. Sangwan, M. C. Hersam, L. Yu, X. Chen, T. F. Heinz, P. Murthy, M. Kroner, T. Smolenski, D. Thureja, T. Chervy, A. Genco, C. Trovatello, G. Cerullo, S. Dal Conte, D. Timmer, A. De Sio, C. Lienau, N. Shang, H. Hong, K. Liu, Z. Sun, L. A. Rozema, P. Walther, A. Alu, A. Marini, M. Cotrufo, R. Queiroz, X.-Y. Zhu, J. D. Cox, E. J. C. Dias, A. R. Echarri, F. Iyikanat, P. Herrmann, N. Tornow, S. Klimmer, J. Wilhelm, G. Soavi, Z. Sun, S. Wu, Y. Xiong, O. Matsyshyn, R. Krishna Kumar, J. C. W. Song, T. Bucher, A. Gorlach, S. Tsesses, I. Kaminer, J. Schwab, F. Mangold, H. Giessen, M. S. Sanchez, D. K. Efetov, T. Low, G. Gomez-Santos, T. Stauber, G. Alvarez-Perez, J. Duan, L. Martin-Moreno, A. Paarmann, J. D. Caldwell, A. Y. Nikitin, P. Alonso-Gonzalez, N. S. Mueller, V. Volkov, D. Jariwala, T. Shegai, J. van de Groep, A. Boltasseva, I. V. Bondarev, V. M. Shalaev, J. Simon, C. Fruhling, G. Shen, D. Novko, S. Tan, B. Wang, H. Petek, V. Mkhitaryan, R. Yu, A. Manjavacas, J. E. Ortega, X. Cheng, R. Tian, D. Mao, D. Van Thourhout, X. Gan, Q. Dai, A. Sternbach, Y. Zhou, M. Hafezi, D. Litvinov, M. Grzeszczyk, K. S. Novoselov, M. Koperski, S. Papadopoulos, L. Novotny, L. Viti, M. S. Vitiello, N. D. Cottam, B. T. Dewes, O. Makarovsky, A. Patane, Y. Song, M. Cai, J. Chen, D. Naveh, H. Jang, S. Park, F. Xia, P. K. Jenke, J. Bajo, B. Braun, K. S. Burch, L. Zhao and X. Xu, *ACS Photon.*, 2025, **12**, 3961–4095.

16 E. P. Nguyen, B. J. Carey, J. Z. Ou, J. Van Embden, E. D. Gaspera, A. F. Chrimes, M. Spencer, S. Zhuiykov, K. Kalantar-Zadeh and T. Daeneke, *Adv. Mater.*, 2015, **27**, 6225–6229.

17 Y. J. Zheng, Y. L. Huang, Y. Chen, W. Zhao, G. Eda, C. D. Spataru, W. Zhang, Y.-H. Chang, L.-J. Li, D. Chi *et al.*, *ACS Nano*, 2016, **10**, 2476–2484.

18 J. J. Thompson, M. Gerhard, G. Witte and E. Malic, *npj 2D Mater. Appl.*, 2023, **7**, 69.

19 S. Mouri, Y. Miyauchi and K. Matsuda, *Nano Lett.*, 2013, **13**, 5944–5948.

20 M. R. Habib, H. Li, Y. Kong, T. Liang, S. M. Obaidulla, S. Xie, S. Wang, X. Ma, H. Su and M. Xu, *Nanoscale*, 2018, **10**, 16107–16115.

21 T. Kuechle, S. Klimmer, M. Lapteva, T. Hamzayev, A. George, A. Turchanin, T. Fritz, C. Ronning, M. Gruenewald and G. Soavi, *Opt. Mater. X*, 2021, **12**, 100097.

22 D. M. Sim, M. Kim, S. Yim, M.-J. Choi, J. Choi, S. Yoo and Y. S. Jung, *ACS Nano*, 2015, **9**, 12115–12123.

23 H. Bretscher, Z. Li, J. Xiao, D. Y. Qiu, S. Refaely-Abramson, J. A. Alexander-Webber, A. Tanoh, Y. Fan, G. Delport, C. A. Williams, S. D. Stranks, S. Hofmann, J. B. Neaton, S. G. Louie and A. Rao, *ACS Nano*, 2021, **15**, 8780–8789.

24 Y. Zhu, Z. Zhang, Y. Wang, S. Sarkar, Y. Li, H. Yan, L. Ishibe-Veiga, A. Bagri, Z. J. Yang, H. Ramsden *et al.*, *J. Phys. Chem. C*, 2025, **129**, 8294–8302.

25 Z. Li, X. Zhou, C. Zhao, L. Xiao and Y. Zhang, *Mater. Chem. Front.*, 2025, **9**, 487–495.

26 B. Luhar, R. Dhankhar, R. V. Nair, A. Soni, N. S. Kamath, S. K. Pal and V. Balakrishnan, *ACS Appl. Nano Mater.*, 2024, **7**, 22350–22359.

27 C. Qin, W. Liu, N. Liu, Z. Zhou, J. Song, S.-h. Ma, Z.-Y. Jiao and S. Lei, *ACS Photon.*, 2022, **9**, 1709–1716.

28 K. T. Munson, R. Torsi, S. Mathela, M. A. Feidler, Y.-C. Lin, J. A. Robinson and J. B. Asbury, *J. Phys. Chem. Lett.*, 2024, **15**, 7850–7856.

29 F. Ceballos, M. Z. Bellus, H.-Y. Chiu and H. Zhao, *ACS Nano*, 2014, **8**, 12717–12724.

30 D. M. de Clercq, J. Yang, M. Hanif, J. Alves, J. Feng, M. P. Nielsen, K. Kalantar-Zadeh and T. W. Schmidt, *J. Phys. Chem. C*, 2023, **127**, 11260–11267.

31 A. R. Cadore, B. L. T. Rosa, I. Paradisanos, S. Mignuzzi, D. De Fazio, E. M. Alexeev, A. Dagkli, J. E. Muench, G. Kakavelakis, S. M. Shinde, D. Yoon, S. Tongay, K. Watanabe, T. Taniguchi, E. Lidorikis, I. Goykhman, G. Soavi and A. C. Ferrari, *2D Mater.*, 2024, **11**, 025017.

32 D.-H. Lien, S. Z. Uddin, M. Yeh, M. Amani, H. Kim, J. W. Ager, E. Yablonovitch and A. Javey, *Science*, 2019, **364**, 468–471.

33 Y. Khan, S. M. Obaidulla, M. R. Habib, Y. Kong and M. Xu, *Appl. Surf. Sci.*, 2020, **530**, 147213.

34 J. Chen, Y. Zhu, H. Guo, Q. Cui, Z. Shi and C. Xu, *J. Lumin.*, 2023, **257**, 119695.

35 H. Wang, C. Zhao, Z. Burešová, F. Bureš and J. Liu, *J. Mater. Chem. A*, 2023, **11**, 3753–3770.

36 M. S. Liu, X. Jiang, S. Liu, P. Herguth and A. K.-Y. Jen, *Macromolecules*, 2002, **35**, 3532–3538.

37 F. Würthner, *Chem. Commun.*, 2004, 1564–1579.

38 B. Kippelen and J.-L. Brédas, *Energy Environ. Sci.*, 2009, **2**, 251–261.

39 T. Weil, T. Vosch, J. Hofkens, K. Peneva and K. Müllen, *Angew. Chem. Int. Ed.*, 2010, **49**, 9068–9093.

40 S. Das, J. Preiß, J. Plentz, U. Brückner, M. von der Lühe, O. Eckardt, A. Dathe, F. H. Schacher, E. Täuscher, U. Ritter *et al.*, *Adv. Energy Mater.*, 2018, **8**, 1801737.

41 S. Jasmin Finkelmeyer and M. Presselt, *Chem. Eur. J.*, 2025, **31**, e202403500.

42 M. L. Hupfer, R. Meyer, T. Deckert-Gaudig, S. Ghosh, A. Skabeev, K. Peneva, V. Deckert, B. Dietzek and M. Presselt, *Langmuir*, 2021, **37**, 11018–11026.

43 S. Jasmin Finkelmeyer, C. Mankel, G. Ansay, A. Elmanova, S. Zechel, Martin D. Hager, U. S. Schubert and M. Presselt, *J. Colloid Interface Sci.*, 2025, **680**, 1090–1100.

44 V. Blum, R. Gehrke, F. Hanke, P. Havu, V. Havu, X. Ren, K. Reuter and M. Scheffler, *Comput. Phys. Commun.*, 2009, **180**, 2175 – 2196.

45 J. P. Perdew, K. Burke and M. Ernzerhof, *Phys. Rev. Lett.*, 1996, **77**, 3865–3868.

46 A. Tkatchenko and M. Scheffler, *Phys. Rev. Lett.*, 2009, **102**, 073005.

47 J. Heyd, G. E. Scuseria and M. Ernzerhof, *J. Chem. Phys.*, 2006, **124**, 219906.

48 O. Ghaebi, T. Hamzayev, T. Weickhardt, M. S. Ramzan, T. Taniguchi, K. Watanabe, C. Cocchi, D. De Fazio and G. Soavi, *ACS Nano*, 2025, **19**, 19027–19034.

49 D.-H. Lien, S. Z. Uddin, M. Yeh, M. Amani, H. Kim, J. W. Ager, E. Yablonovitch and A. Javey, *Science*, 2019, **364**, 468–471.

50 Z. Li, F. Rashvand, H. Bretscher, B. M. Szydłowska, J. Xiao, C. Backes and A. Rao, *J. Phys. Chem. C*, 2022, **126**, 21681–21688.

51 J. Wierzbowski, J. Klein, F. Sigger, C. Straubinger, M. Kremser, T. Taniguchi, K. Watanabe, U. Wurstbauer, A. W. Holleitner, M. Kaniber *et al.*, *Sci. Rep.*, 2017, **7**, 12383.

52 Y. Kong, S. M. Obaidulla, M. R. Habib, Z. Wang, R. Wang, Y. Khan, H. Zhu, M. Xu and D. Yang, *Mater. Horiz.*, 2022, **9**, 1253–1263.

53 T. Völzer, A. Schubert, E. von der Oelsnitz, J. Schröer, I. Barke, R. Schwartz, K. Watanabe, T. Taniguchi, S. Speller, T. Korn *et al.*, *Nanoscale Adv.*, 2023, **5**, 3348–3356.

54 K. Momma and F. Izumi, *J. Alloys Compd.*, 2011, **44**, 1272–1276.

55 F. L. Hirshfeld, *Theor. Chem. Acta*, 1977, **44**, 129–138.

56 J. Krumland and C. Cocchi, *Electron. Struct.*, 2021, **3**, 044003.

57 A. Elmanova, B. O. Jahn and M. Presselt, *J. Phys. Chem. A*, 2024, **128**, 9917–9926.

58 S. H. Amsterdam, T. K. Stanev, L. Wang, Q. Zhou, S. Irgen-Gioro, S. Padgaonkar, A. A. Murthy, V. K. Sangwan, V. P. Dravid, E. A. Weiss, P. Darancet, M. K. Y. Chan, M. C. Hersam, N. P. Stern and T. J. Marks, *J. Am. Chem. Soc.*, 2021, **143**, 17153–17161.

59 F. Herrmann, B. Muhsin, C. R. Singh, S. Shokhovets, G. Gobsch, H. Hoppe and M. Presselt, *J. Phys. Chem. C*, 2015, **119**, 9036–9040.

60 Y. T. Gerase, A. Elmanova, S. J. Finkelmeyer, A. Dellith, J. Dellith, J. Guthmuller, O. Ryabchykov, T. Bocklitz, F. G. Fabozzi, N. Severin, S. Hecht, L. Renn, J. Borchert, R. T. Weitz, J. Müller, C. T. Koch and M. Presselt, *Adv. Mater.*, 2025, e09825.